Earth, Planets and Space

FULL PAPER Open Access

Subsurface magma movement inferred from extensometer and tiltmeter records during the early stage of the 2018 Shinmoe-dake eruptions, Japan

Koki Yoshinaga[1*], Takeshi Matsushima[2], Hiroshi Shimizu[2], Yusuke Yamashita[3], Ken'ichi Yamazaki[3], Shintaro Komatsu[3] and Satoshi Fujiwara[4]

Abstract

We infer the temporal changes in the pressure sources that induced crustal deformation during the 2018 Shinmoe-dake eruption using strain and tilt observations and discern that the deep magmatic activity associated with the early stage of this eruption began approximately 19 h earlier than the previously defined onset of magmatic activity. Distinct tilt changes were observed from around 09:00 on 6 March to 12:00 on 8 March 2018 (JST), coincident with observed lava outflow into the crater and lava dome formation. Existing studies have attributed this tilt change to the onset of the deflation of a spherical pressure source located at ~ 7 km bsl (below sea level) to the northwest of Shinmoe-dake. Here we examine strain and tilt data that were acquired in the Kirishima volcanic group, and we find that the distinct changes in the measured strain at Isa-Yoshimatsu Observatory began at around 14:00 on 5 March. This change can be explained by the deflation of a spherical pressure source, thereby suggesting that the onset of magma ascent was earlier than previously thought. The time variation in the spherical pressure source is estimated using the time-dependent inversion of the Ensemble Kalman Filter; the deflation source ascended from ~ 11 to 7 km bsl during Phase 1 (14:00 on 5 March to 06:00 on 6 March) and descended from 7 to 8 km bsl during Phase 2 (06:00 on 6 March to 12:00 on 8 March). Interferometric synthetic aperture radar analysis suggests that a dike intrusion had occurred just below Shinmoe-dake crater until 5 March, and this inflatable crustal deformation is attributed to the emplacement of residual volcanic fluids from the 2011 eruption. It is also known that the surface eruptive activity increased during Phase 1, including an increase in ash venting from the night of 5 March. These strain and tilt observations, therefore, suggest that magma ascended from ~ 11 km bsl to the magma reservoir at 7 km bsl during Phase 1, followed by a deflation of the magma reservoir during Phase 2 due to the large magma supply to the surface.

Keywords 2018 Shinmoe-dake eruption, Strain, Tilt, Time-dependent inversion, Magma plumbing system, Extensometer, Magma effusion, Ensemble Kalman Filter, Subsurface magma movement

*Correspondence:
Koki Yoshinaga
yoshinaga.koki@sevo.kyushu-u.ac.jp
Full list of author information is available at the end of the article

Graphical Abstract

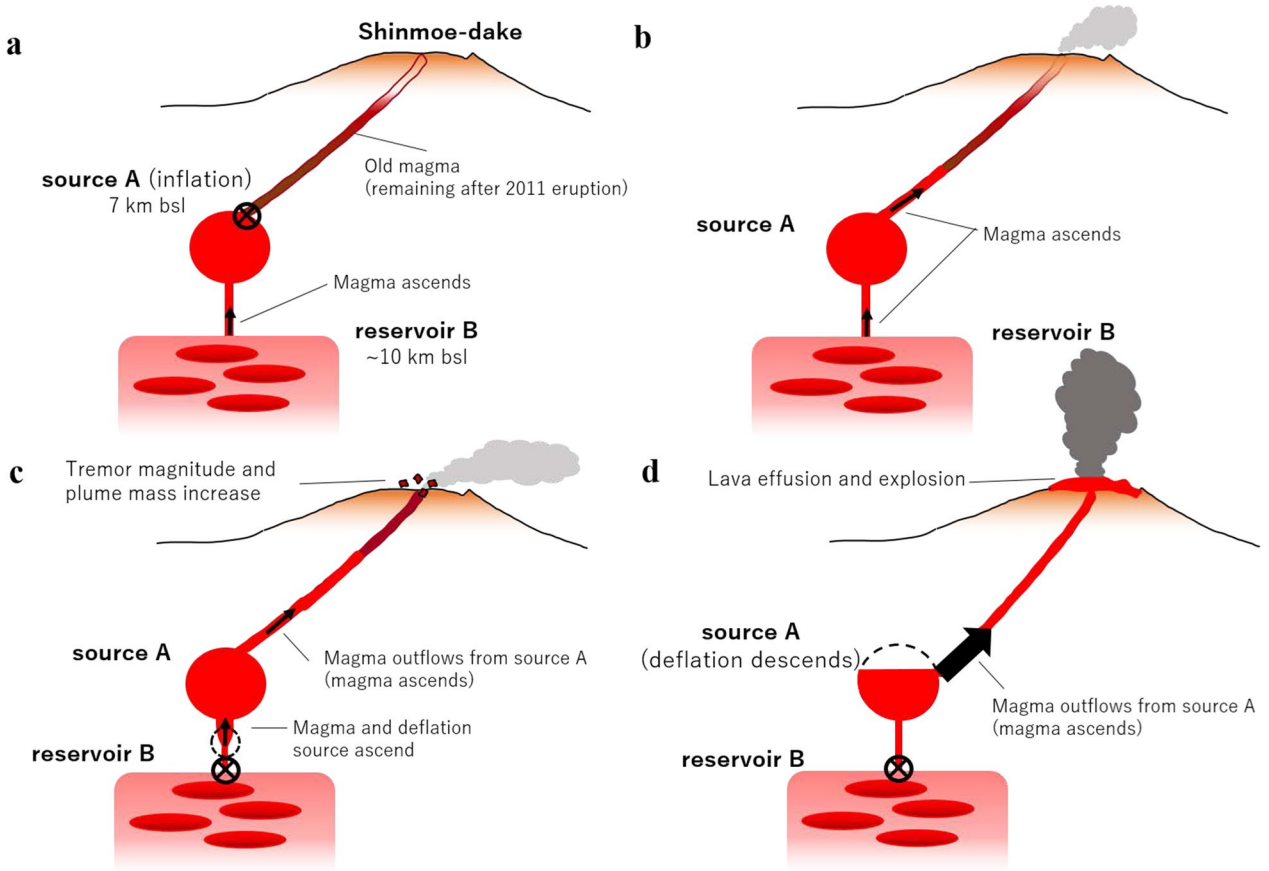

Introduction

The ability to predict a volcanic eruption and/or elucidate its eruption mechanism is heavily contingent on understanding how magma moves between the summit crater and magma reservoir in a given volcanic system. For example, it is known that the crater-directed tilt at Kilauea volcano, Hawaii, increases before an eruption and decreases during each eruption (Tanner and Calvari 2012). This type of episodic inflation–deflation cycle of the volcanic edifice, whereby the subsurface magma reservoir inflates owing to pressurization before an eruption and then deflates after the eruption begins, is commonly observed at many active volcanoes (e.g., Genco and Ripepe 2010; Bonforte et al. 2008).

However, it is unclear whether effusive eruptions are triggered by pressure changes in either the upper magma plumbing system or the deep magma reservoir. This is because observations with good temporal resolution and observational accuracy are necessary to capture magma movement in detail, and the availability of such high-quality spatial and temporal observations at active volcanoes is currently limited (Nakamichi and Aoyama 2016).

The Kirishima volcanic group consists of over 20 northwest–southeast-aligned craters in the southwestern part of Kyushu. Shinmoe-dake, Ohachi, Iwo-yama, and Ohata-ike are currently the most active craters, and the Japan Meteorological Agency (JMA) carefully monitors these four craters and regularly issues volcanic eruption warning information based on their associated volcanic activity (FDMO and KLMO 2023). Shinmoe-dake, which is the subject of this study, is an andesitic volcano that has erupted frequently in recorded history, and pyroclastic flows were observed during the 1716–1717 eruptions. Small phreatic eruptions also occurred in 1991, 2008, and 2010 (Kato and Yamasato 2013), and the most recent major magmatic eruptions occurred in 2011 and 2018. The 2011 eruption was the first magmatic eruption in about 300 years; lava outflow into the crater was

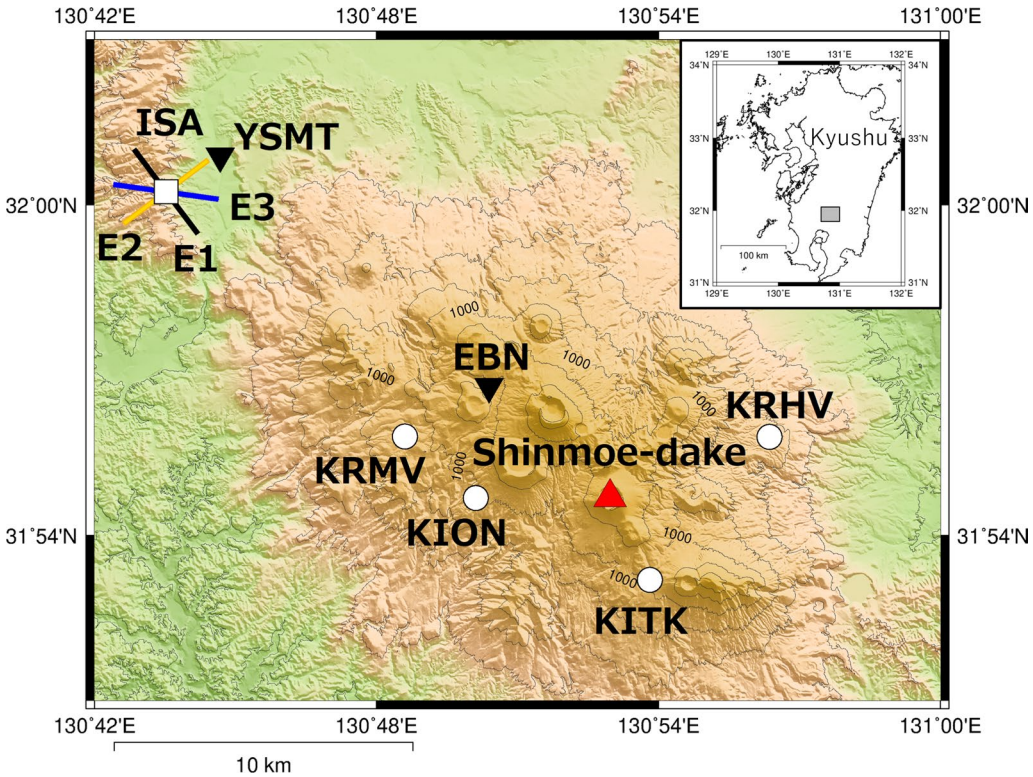

Fig. 1 Map of the Kirishima volcanic group in Kyushu Island, showing the locations of Shinmoe-dake crater (triangle) and the observation sites. The square, circles, and inverted triangles mark the locations of the extensometer site (ISA), tiltmeter sites (KION, KITK, KRHV, and KRMV), and rain gauges, respectively

confirmed after three sub-Plinian eruptions (Kato and Yamasato 2013; Nakada et al. 2013). The 2018 eruption began on 1 March and was marked by continuous ash venting during its early stage, followed by both the first observations of lava outflow into the crater and the first vulcanian eruption occurring on 6 March; volcanic glow was also observed at night (JMA 2018).

The Kirishima volcanic group, including Shinmoe-dake, has been the subject of multiple geological and geophysical investigations, resulting in various research studies on the physics, chemistry, and petrology of the 2011 eruption (e.g., Nakao et al. 2013; Suzuki et al. 2013; Tajima et al. 2022). Continuous monitoring of the volcanic activity is primarily undertaken using Global Navigation Satellite System (GNSS), tilt, and strain (extensometer) observations. Geodetic analyses have estimated that the magmatic source of the 2011 and 2018 eruptions was a spherical pressure source at 7–10 km below sea level (bsl) to the northwest of Shinmoe-dake (Ueda et al. 2013; Nakao et al. 2013; JMA 2018).

The 2011 eruption was marked by major strain changes at Isa-Yoshimatsu Observatory during the sub-Plinian eruptions and lava outflows, which indicated deflation of the pressure source and subtle strain changes a few hours before the three sub-Plinian eruptions (Yamazaki et al. 2013). The GNSS baseline length began to increase around December 2009 as a preparatory process for the 2011 eruption, and the strain changed between 15 and 17 December 2009, with these geodetic changes attributed to magma supply from a deep magma reservoir (Yamazaki et al. 2020). GNSS observations can detect subsurface volume changes with an accuracy of the order of 10^5–10^6 m^3, whereas extensometers can detect those with an accuracy of the order of 10^4 m^3 at depth (several kilometers or deeper) (Yamazaki et al. 2013). Furthermore, extensometers can continuously obtain 1-Hz data with this high accuracy. Therefore, strain measurements are important for estimating deep magma movement in active volcanic environments.

All of these strain-based research results focused on the 2011 eruption, and these geodetic considerations have not been particularly advanced for the 2018 eruption. This study aims to elucidate the mechanism of the Kirishima magma plumbing system by examining the extensometer and tiltmeter data from the 2018 eruption in detail. We specifically investigate how the pressure source changed over time during the early stage of the

2018 eruption by conducting a time-dependent inversion of the strain and tilt data.

Strain and tilt observations and corrections

The strain data are from the extensometers that are maintained by the Disaster Prevention Research Institute, Kyoto University, at Isa-Yoshimatsu Observatory (ISA; 32.0040°N, 130.7254°E; Fig. 1), ~ 18.5 km northwest of Shinmoe-dake crater. The extensometers consist of 30-m-long Super Invar rods (which are insensitive to temperature variations) that have been installed in three horizontal tunnels (E1, E2, and E3; Yamazaki et al. 2013). The displacement of the free end of a given Super Invar rod is measured at a 1-s interval and divided by its length to calculate the strain. The precision of the strain measurement data at ISA is 1×10^{-9} in each direction.

The tilt data are from KITK (31.8865°N, 130.8970°E) and KION (31.9113°N, 130.8352°E), and KRMV (31.9300°N, 130.8101°E) and KRHV (31.9298°N, 130.9394°E), which are maintained by JMA and the National Research Institute for Earth Science and Disaster Prevention (NIED), respectively. Tiltmeters KITK and KION are deployed at the bottom of 100-m-deep boreholes to obtain continuous 1-Hz tilt measurements (VDSVD 2014). Tiltmeters KRMV and KRHV are part of the NIED volcano observation network (V-net) and are deployed at the bottom of 200-m-deep boreholes to obtain continuous 20-Hz tilt measurements (Ueda et al. 2013).

The high precision of the extensometers and tiltmeters means that non-volcanic crustal deformation is introduced to the data as noise owing to tides, rainfall, and instrument drift. Therefore, we used the following procedure to correct the data. We first resampled the strain and tilt data into 1-min bins by calculating the arithmetic mean, and then removed the tidal component using BAYTAP-G (Ishiguro et al. 1984). We then removed the rainfall component following the approach outlined in Ueda et al. (2010) and Kimura et al. (2015). A three-layer tank model is assumed for the subsurface structure, whereby the water level in the i-th aquifer at time t_n is assumed to be $y_i(t_n)$, which is assumed to vary according to the following equation:

$$\begin{aligned} y_i(t_{n+1}) &= (1-r_i)y_i + (t_n)\mathrm{P}(t_n) \text{ for } i=1 \\ y_i(t_{n+1}) &= (1-r_i)y_i(t_n) + r_{i-1}y_{i-1}(t_n) \text{ for, } i \neq 1, \end{aligned} \tag{1}$$

where r_i is the infiltration rate of layer i and $\mathrm{P}(t_n)$ is the precipitation at time t_n. The crustal deformation due to rainfall $H(t_n)$ is calculated using the response function A_i :

$$H(t_n) = \sum_{i=1}^{3} A_i y_i(t_n) \tag{2}$$

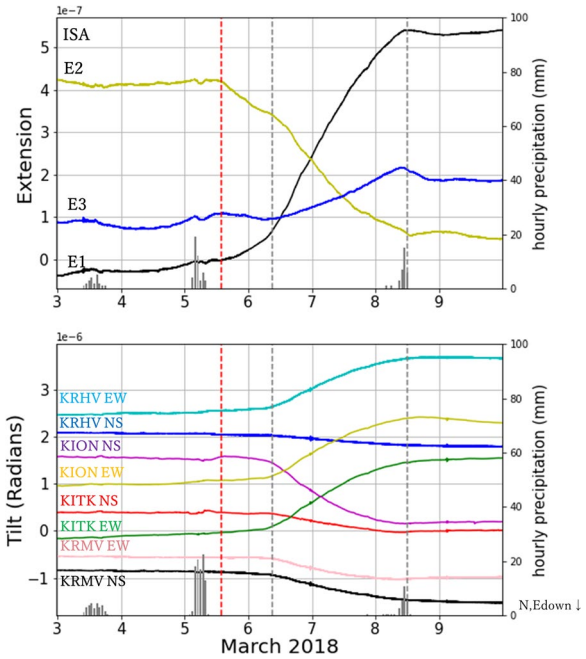

Fig. 2 Strain (extension; upper panel) and tilt (lower panel) time series for the 3–9 March 2018 period, after removal of the tidal, precipitation, and instrument drift components. The gray bars at the bottom of each panel represent hourly precipitation measurements at Yoshimatsu (YSMT, Fig. 1; upper panel) and Ebino (EBN, Fig. 1; lower panel). Gray dashed lines denote the start and end times of clear changes in the tiltmeter observations (09:00 on 6 March to 12:00 on 8 March) based on JMA (2018). The red dashed line denotes the start time of clear changes in the extensometer observations (14:00 on 5 March)

The crustal deformation time series after the precipitation correction $D\prime(t_n)$ can be expressed by subtracting $H(t_n)$ from the times series before the precipitation correction $D(t_n)$:

$$D\prime(t_n) = D(t_n) - H(t_n) \tag{3}$$

The unknown parameters, r_i and A_i, were determined from our crustal deformation observations (1–10 May 2018 period) via a grid search. These parameters were assumed to be the optimal values that minimized the following objective function f:

$$f = \sum_{t_n=0}^{T} \left| D'(t_n) - D'(t_n - 24) - T_r \right|, \tag{4}$$

where T_r is the trend coefficient from period 0 to T. Note that f in Eq. (4) will be zero if the rainfall component is removed completely.

We used the precipitation data from a rain gauge that was installed in Yoshimatsu Town by Kagoshima Prefecture (YSMT, Fig. 1) for ISA, and from the JMA Ebino station (EBN, Fig. 1) for the tiltmeters. Finally, we removed

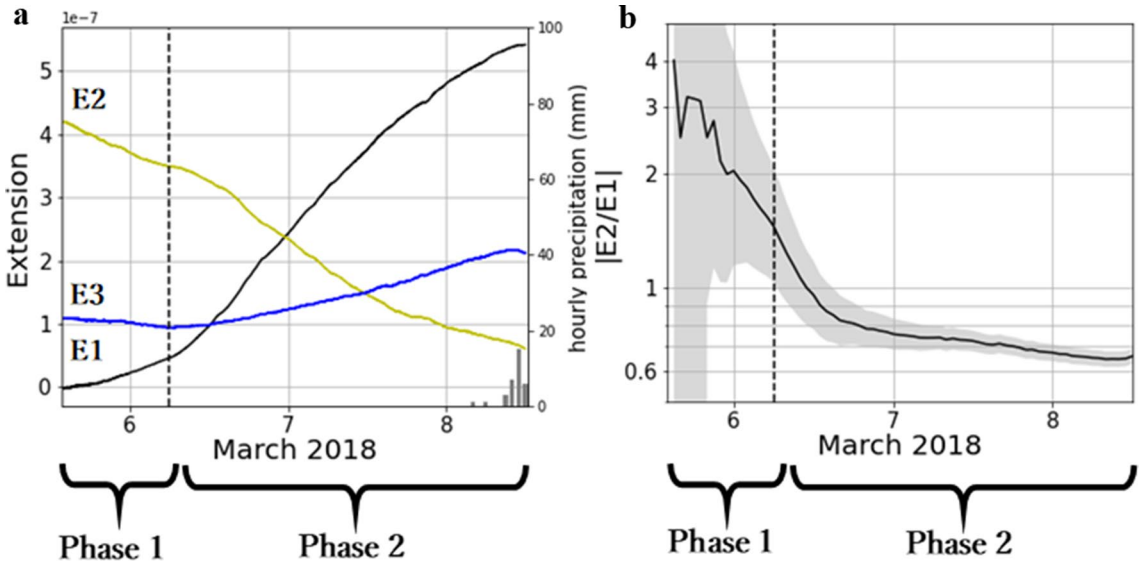

Fig. 3 **a** Strain (extension) time series at ISA from 14:00 on 5 March to 12:00 on 8 March. Black dashed lines in **a** and **b** mark the boundary between Phases 1 and 2 of the eruption (06:00 on 6 March). **b** Observed |E2/E1| ratio of the extensometers at ISA from 14:00 on 5 March to 12:00 on 8 March. The gray area denotes the error range of observed |E2/E1| ratio calculated from the observation errors of E1 and E2

the instrument drift from the tide- and precipitation-corrected time series by detrending the time series using a linear approximation. The raw and corrected strain and tilt time series analyzed in this study are provided in Additional file 1: Fig. S1.

Strain and tilt changes during lava effusion

The 2018 Shinmoe-dake eruption began on 1 March with ash venting and the formation of an ash cloud at the summit crater. Ash venting continued until 5 March, during which time the volcano is thought to have been sweeping away material from the 2011 eruption that was present in the upper part of the magma plumbing system (Matsumoto and Geshi 2021). The first visual observation of lava outflow into the crater was 13:35 on 6 March (FDMO and KLMO 2018), with synthetic aperture radar (SAR) analysis estimating that lava outflow began on the morning of 6 March (NIED 2018), although the exact start time is unknown. The first explosive eruption occurred on 6 March, with an additional 18 and 16 eruptions on 6 and 7 March, respectively. The SO_2 flux also increased dramatically to 34,000 tons/day on 7 March (JMA 2018). The lava dome in the crater continued to grow significantly through 8 March, with a final estimated dense-rock-equivalent (DRE) volume of $\sim 1.5 \times 10^7$ m^3 (The Asia Air Survey Co. Ltd. et al.

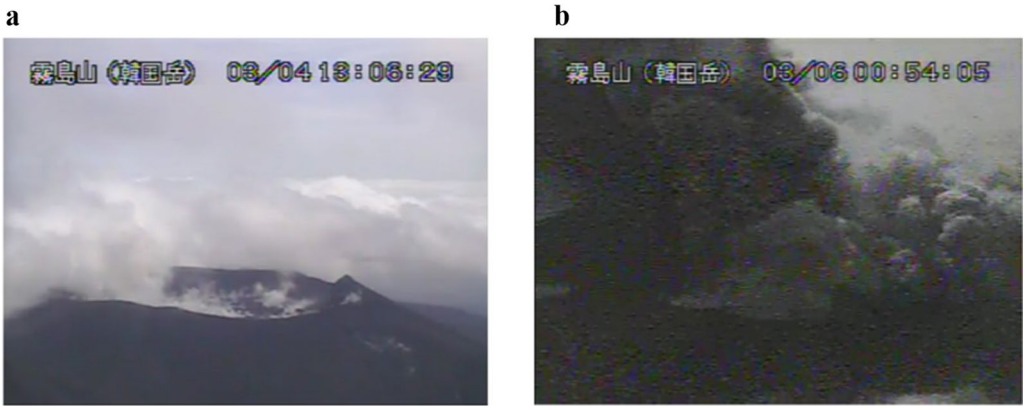

Fig. 4 Still images from the video data recorded at Karakunidake station (operated by the JMA) during the 2018 eruption. **a** 13:06 on 4 March. **b** 00:54 on 6 March

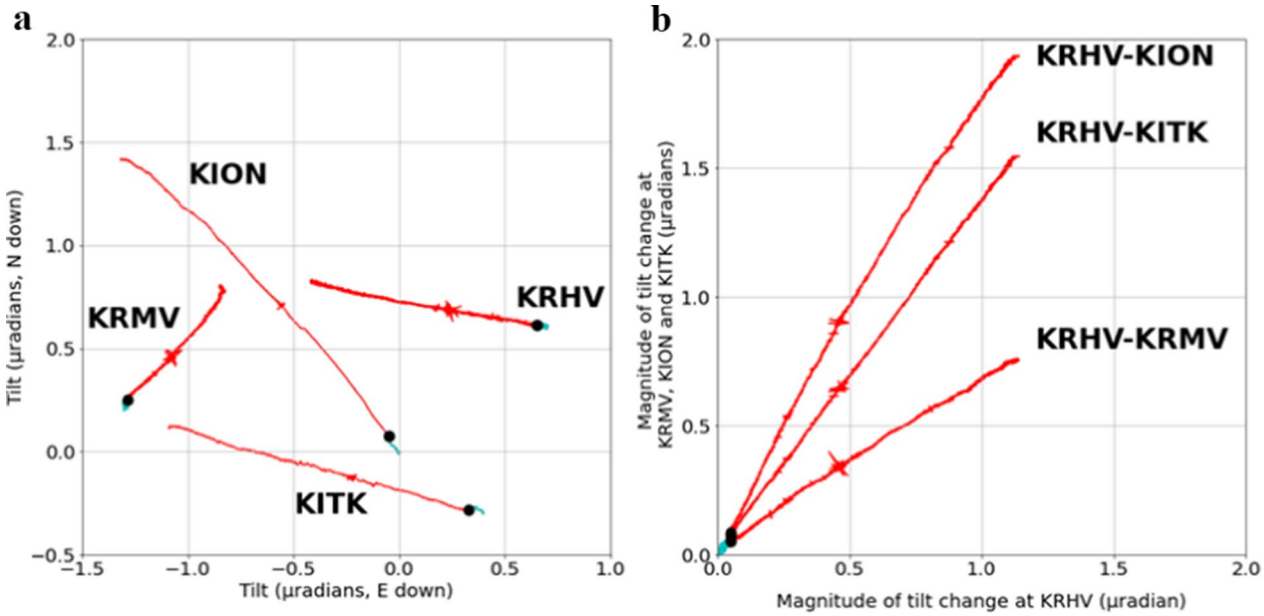

Fig. 5 **a** Variations in the tilt-down vector direction recorded at each station. The blue lines are the vector directions that were recorded during Phase 1, and the red lines are the vector directions that were recorded during Phase 2. **b** Relationship between the change in tilt magnitude at KRHV and the other stations (KRMV, KION, and KITK)

2018). We, therefore, assume that the climax phase of the 2018 eruption occurred during the 6–8 March period.

The crustal deformation data for the Kirishima area show that there were significant changes in both strain and tilt during the 6–8 March period (Fig. 2). The JMA (2018) reported that distinct tilt changes were observed in the tiltmeters from around 09:00 on 6 March to 12:00 on 8 March, with our tiltmeter observations (KITK, KION, KRMV, and KRHV in Fig. 2) also detecting distinct changes during the same time period.

However, the strain time series at ISA shows that the strain change started around 14:00 on 5 March (Fig. 2). Although 47 mm of rainfall was observed at YSMT (Fig. 1) on the morning of 5 March, we interpret this strain change as volcanic crustal deformation, since we applied tidal, rainfall, and instrument drift corrections using the method described in the "Strain and tilt observations and corrections" section. Although it was previously thought that distinct crustal deformation occurred from around 09:00 on 6 March to 12:00 on 8 March based on tiltmeter observations (JMA, 2018), our analysis of the tiltmeter data, in combination with the strain data at ISA, indicates that crustal deformation actually began at around 14:00 on 5 March.

Phases of the 2018 eruption

We examined the time period of observed crustal deformation in detail to better understand the evolution of the 2018 Shinmoe-dake eruption. Using the strain time series from 14:00 on 5 March to 12:00 on 8 March (Fig. 3a), we noted a significant change in each strain component after around 06:00 on 6 March and set this time as the boundary between two phases of crustal deformation during the eruption: Phase 1 (from 14:00 on 5 March to 06:00 on 6 March) and Phase 2 (from 6:00 on 6 March to 12:00 on 8 March). The magnitude of volcanic tremors increased from around 21:00 on 5 March, with the ejection of larger cinders from around 24:00 on 5 March until the early morning of 6 March. Furthermore, video images of the Shinmoe-dake crater (Fig. 4) recorded an increase in the amount of plumes from around 23:00 on 5 March. These observations indicate that explosive activity had already commenced during Phase 1.

The time series of the |E2/E1| ratio at ISA shows that the |E2/E1| ratio rapidly dropped from 3–4 to ~ 1.5 during Phase 1, whereas it rapidly stabilized to 0.6–0.8 during Phase 2 (Fig. 3b). Furthermore, the tilt vectors and the relationship between the changes in tilt magnitude of the observation stations (Fig. 5) were constant during Phase 2. The strain component ratio and tilt vector direction should remain constant if a single pressure source continues to inflate or deflate the same volume. This indicates that there may have been a change in the position of the pressure source between Phases 1 and 2. Therefore, it is necessary to estimate the detailed positional changes of the pressure source (i.e., magma movement) using the continuous extensometer and tiltmeter records.

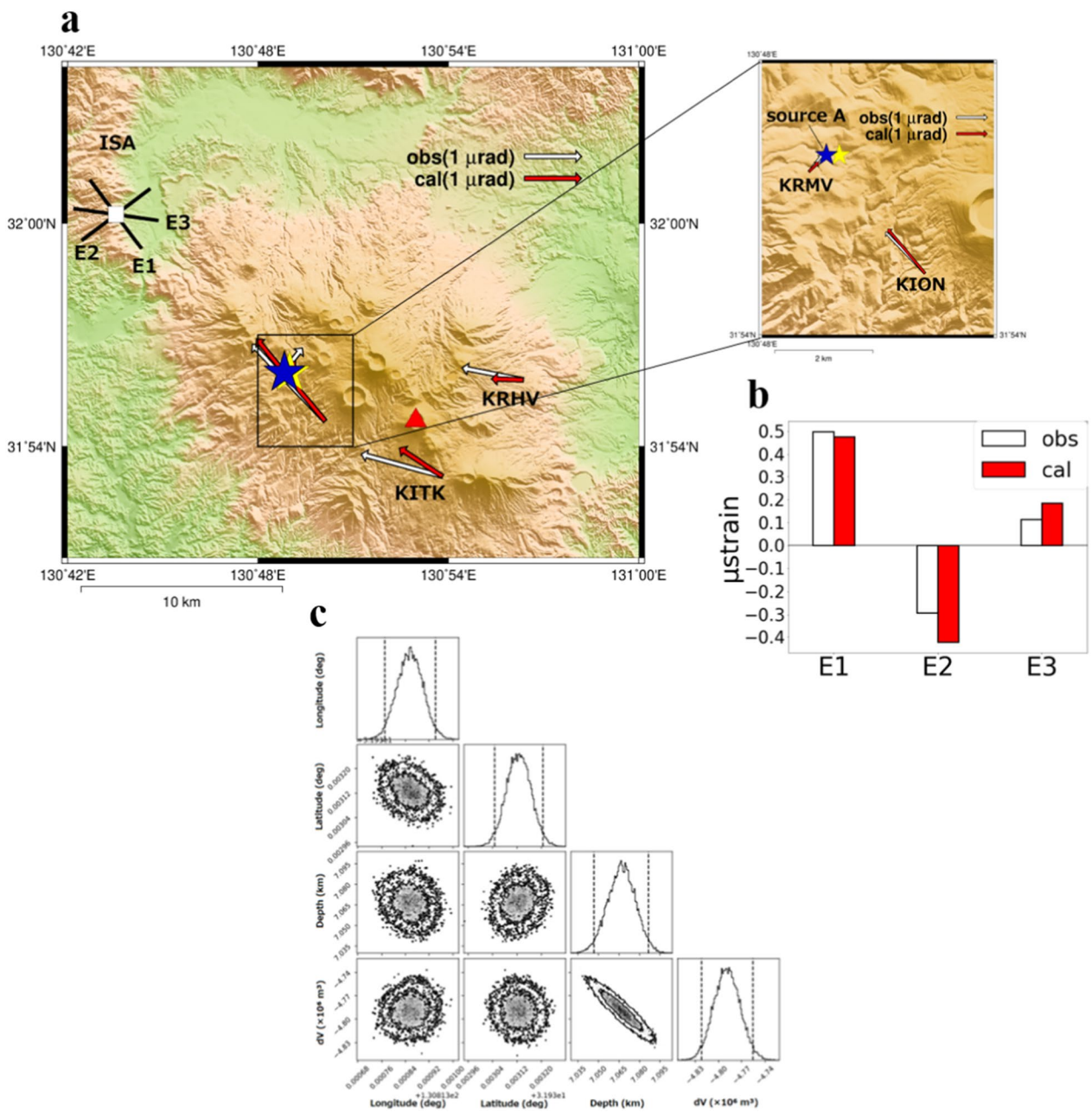

Fig. 6 **a** Location of the obtained spherical source (source A, blue star) during Phase 2 and a comparison of the observed (white) and calculated (red) downward tilts. The yellow star is the Mogi model source location that was determined by JMA (2018). **b** Comparison of the observed (white) and calculated (red) E1, E2, and E3 strains at ISA. The error bars are for the 95% confidence level but are too small to discriminate in the plot. **c** Corner plot for the MCMC inversion for the Phase 2 source parameters. Only the parameters shown in Table 1 are plotted. Dashed lines in the diagonal plots represent the bounds for the 95% confidence level

Source estimation

Phase 2 source

We previously considered that the location and shape of the pressure source remained almost constant and continued to deflate during Phase 2. Therefore, we first estimated the parameters of this pressure source, including its horizontal position and shape, using the crustal deformation data from Phase 2 prior to estimating the Phase 1 source parameters. Here, we only use the Phase 2 data for the source estimation to apply the resultant fixed horizontal position to the time-dependent inversion in the "Time-dependent inversion for the Phase 1 and Phase

Table 1 Comparison of the estimated model parameters in this study and JMA (2018)

	Latitude (°N)	Longitude (°E)	Depth (km)	dV ($\times 10^6$ m^3)
Spherical Source (source A)	31.9331	130.8139	7.1	− 4.8
Mogi model Source (JMA 2018)	31.9331	130.8167	7.2	− 7.1

2 source parameters using the ensemble Kalman filter" subsection. We adopted an integrated Markov Chain Monte Carlo (MCMC) and inverse analysis approach as the calculation method. More specifically, the optimal solution determined by the MCMC method was used as the initial value for the nonlinear inversion to improve the efficiency of the calculation. The same MCMC method as in Munekane et al. (2016) was employed in the calculation, whereby the posterior probability distributions of the pressure source parameters were randomly sampled. We applied the varying depth model (Williams and Wadge 1998, 2000) in this analysis and assumed a half-infinite homogeneous elastic solid.

Three sub-Plinian eruptions and lava outflow were confirmed during the 2011 Shinmoe-dake eruption, and a single Mogi model pressure source (Mogi 1958) was estimated to the northwest of the crater at 7–10 km bsl based on the GNSS and tiltmeter crustal deformation observations (Nakao et al. 2013; Ueda et al. 2013). The Mogi model source was estimated at almost the same location for the 2018 eruption (JMA 2018), and this pressure source is inferred to have been a magma reservoir that repeatedly accumulates and supplies magma to Shinmoe-dake crater. Therefore, we used a finite spherical pressure source model (McTigue 1987) because this model assumes that a pressure source isotropically inflates and deflates, as in the Mogi model.

The optimal solution in our calculation is a deflation source at 7.1 km bsl to the northwest of Shinmoe-dake crater during Phase 2 (source A, Fig. 6a). Both the horizontal position and depth are determined in almost the same location as the deflation source that was estimated using GNSS data (JMA 2018), but with a smaller volume change (Table 1). The reason for the difference in volume change is that the analysis period for the GNSS-based volume is 1–10 March, whereas the analysis period for the strain- and tilt-based volume is only 6–8 March.

Time-dependent inversion for the Phase 1 and Phase 2 source parameters using the ensemble Kalman filter

We tested two models with different numbers of set spherical pressure sources for the Phase 1 source based on the Phase 2 source (source A) estimation results due to the observed |E2/E1| changes during Phase 1.

We first considered the case of two spherical pressure sources, whereby magma migration between the two sources is assumed during Phase 1. However, we found that this model was not appropriate for this study, as explained below. We assumed that source A was one of the two pressure sources, such that its position (horizontal position and depth) was fixed; the volume change of source A and all of the parameters of the other pressure source were then estimated via the MCMC method. These parameters were estimated via the deflation due to two pressure sources, sources A and A'. Source A' was modeled ~ 7 km to the northwest and 3 km shallower than source A; the modeled parameters for these two sources are listed in Table 2. Magma movement between these two pressure sources was unlikely during Phase 1 due to the modeled locations of these two pressure sources relative to Shinmoe-dake crater. Therefore, the two-source model is not suitable for modeling Phase 1 of the 2018 eruption.

We then considered the case of a single spherical pressure source with an ascending deflation front during Phase 1. Note that we considered a single stationary spherical pressure source that deflated during Phase 2 ("The Phase 2 source" subsection). Therefore, we modeled a spherical pressure source with a continuously ascending deflation front during Phase 1. The results of the Phase 2 pressure source estimation show that the E1 and E2 azimuths at ISA are generally radial and transverse to source A, respectively. If we use the Mogi model for simplicity and assume that E1 and E2 are radial and transverse to the Mogi model, respectively, then the |E2/E1| ratio can be expressed as:

$$\left|\frac{E2}{E1}\right| \approx \left|\frac{r^2+h^2}{-2r^2+h^2}\right|, \tag{5}$$

Table 2 Estimated model parameters during Phase 1 for the case of two spherical sources

	Latitude (°N)	Longitude (°E)	Depth (km)	dV ($\times 10^6$ m^3)
Source A (sphere)	31.9331 (fixed)	130.8139 (fixed)	7.1 (fixed)	− 0.27
Source A' (sphere)	31.9713	130.7465	3.8	− 0.04

where r is the horizontal distance from ISA to the source and h is the depth of the source. If we assume that r is constant over time, then the observed convergence of |E2/E1| to ~ 0.7 from 3–4 during the period from the onset of Phase 1 to the early stage of Phase 2 (Fig. 3b) corresponds to a decrease in depth h. Therefore, if we assume a single pressure source during Phase 1, then the continuous ascension of the deflation front to source A can be used explain the strain observations.

We specifically want to know how the pressure source changed over time from Phase 1 to Phase 2. Here, we introduced a time-dependent inversion analysis (Segall and Matthews 1997) using the ensemble Kalman filter (EnKF) to solve this problem.

We solved two equations, the equation of state and the observation equation, during our time-dependent inversion analysis. The equation of state describes the change in model parameters between the current and previous epochs, and the observation equation links the model parameters to the observed values. We dealt with the nonlinear problem of simultaneously estimating the source location and pressure change by treating the source parameters as an ensemble. Here, the equation of state is written as:

$$\boldsymbol{X}^l_{k|k-1} = \boldsymbol{F}\left(\boldsymbol{X}^l_{k-1|k-1}\right) + \boldsymbol{\delta}^l_k, \tag{6}$$

where the superscript l indicates the lth ensemble member, $\boldsymbol{X}^l_{k|k-1}$ is the state-space vector at time k, $\boldsymbol{X}^l_{k-1|k-1}$ is the state-space vector at time k–1, and $\boldsymbol{\delta}^l_k$ is the system noise. The observation equation is written as:

$$\boldsymbol{y}_k = \boldsymbol{h}\left(\boldsymbol{X}^{true}_k\right) + \boldsymbol{\varepsilon}_k, \tag{7}$$

where $\boldsymbol{y}_k$ is the cumulative crustal deformation vector, the superscript *true* indicates that $\boldsymbol{X}_k$ is a true value, and $\boldsymbol{\varepsilon}_k$ is the observation error. The Kalman filter is defined from Eqs. (6) and (7) as:

$$\boldsymbol{X}^l_{k|k} = \boldsymbol{X}^l_{k|k-1} + \overline{\boldsymbol{K_K}}\left(\boldsymbol{y}_k + \boldsymbol{r}^l_k - \boldsymbol{h}\left(\boldsymbol{X}^l_{k|k-1}\right)\right), \tag{8}$$

where $\overline{\boldsymbol{K_K}}$ is the Kalman gain and $\boldsymbol{r}^l_k$ is the pseudo-observation error. Note that the l-th state space vector $\boldsymbol{X}^l_k$ is expressed as Eq. (9), since the cumulative crustal deformation is used as data:

$$\boldsymbol{X}^l_k = \begin{bmatrix} \boldsymbol{m}^l_k \circ \\ \boldsymbol{c}^l_{k-1} \circ \end{bmatrix} \tag{9}$$

where $\boldsymbol{m}^l_k$ is the model parameter at the current epoch and $\boldsymbol{c}^l_{k-1}$ is the cumulative crustal deformation up to the previous epoch.

Munekane and Oikawa (2017) have demonstrated the effectiveness of using EnKF in the time-dependent inversion analysis of volcanic crustal deformation problems. Here, the depth and pressure of the spherical source were both varied over time. We first defined a set of pressure source parameters and simulated the source parameters using the same arrangement of actual observation stations that obtained the real data prior to performing the calculations using the real data (Additional file 1: Fig. S2). After calculating the strain and tilt changes from these set pressure source parameters via a forward analysis, we added white noise levels of 1×10^{-8} and 2×10^{-8} to the simulated strain and tilt data to obtain the pseudo-observed values. The trend of the pressure source depth over time was consistent with the simulation data, and the estimated volume change was within the margin of error. These results confirmed the effectiveness of the time-dependent inversion using EnKF.

The model setup for the real data was as follows. A 70-h analysis period was defined from the start of Phase 1 to the end of Phase 2 (14:00 on 5 March to 12:00 on 8 March), with each epoch being 1 h in length, resulting in 70 epochs. The total number of data observations was 770, as the tilt data consisted of two-component observations from four stations and the strain data consisted of three-component data from one station. Here, we assumed that the crustal deformation was caused by the movement of a finite spherical pressure source, which was used as the source model. The horizontal position (latitude and longitude) of the spherical pressure source was fixed based on the estimated position during Phase 2, and the depth and pressure change (i.e., volume change) were then treated as the unknown parameters that were estimated at each epoch, resulting in 140 unknown parameters for the entire analysis period. We fixed the horizontal position in the model owing to the limited number of observation data and the fact that the depth provides more important information on the pressure source movement than the horizontal position in this study. We also employed a backward smoothing process with fixed-lag smoothing in the inversion, whereby we set the smoothing length to 10 epochs.

It is necessary to determine the optimal balance between the smoothness and residuals of the unknown parameters to ensure the convergence and reliability of the inversion results. Here, we introduced α_{dep} and α_{cap} as smoothing parameters for the depth and pressure change, respectively, since these two parameters are free in the inversion. The α_{dep} and α_{cap} were incorporated into Eq. (7) to obtain:

$$\begin{bmatrix} \boldsymbol{y}_k \\ 0 \\ 0 \end{bmatrix} = \begin{bmatrix} h \\ \alpha_{dep}\boldsymbol{H_{dep}} \\ \alpha_{cap}\boldsymbol{H_{cap}} \end{bmatrix} \left(\boldsymbol{X}^{true}_k\right) + \boldsymbol{\varepsilon}_k \tag{10}$$

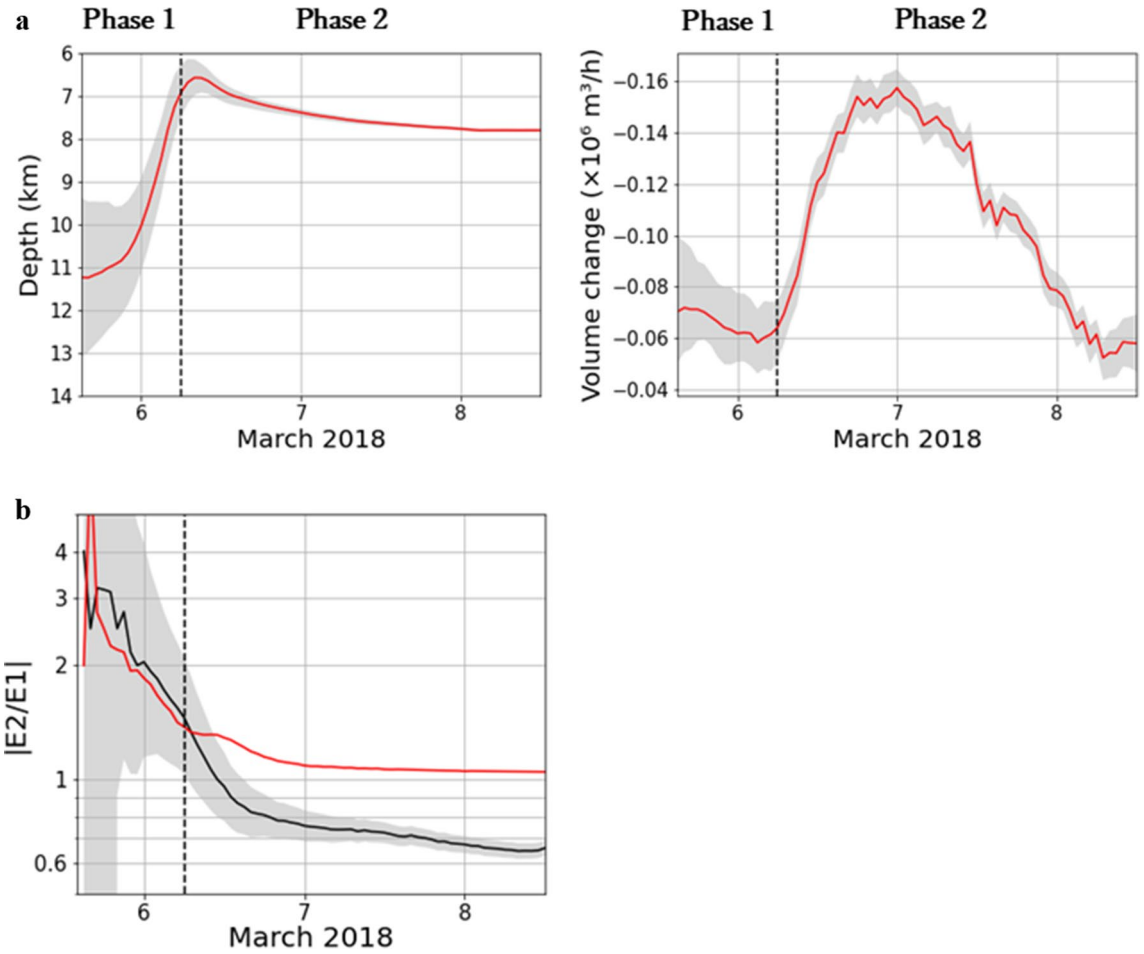

Fig. 7 **a** Estimated depth and volume change for a source using EnKF. Red lines are calculated values, and gray areas correspond to the 95% confidence level. **b** Comparison of the observed (black) and calculated (red) |E2/E1| ratios at ISA

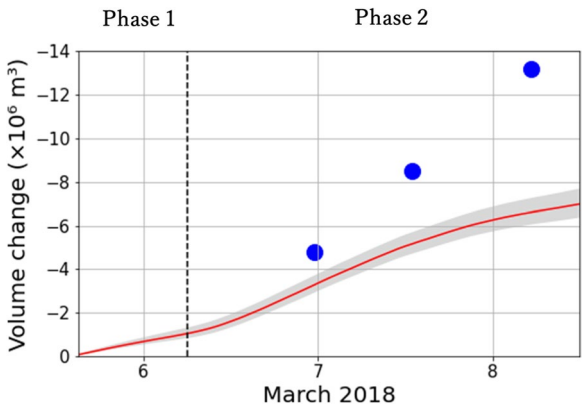

Fig. 8 Comparison of the geodetic volume change (V_G) and DRE volume (V_D) during Phases 1 and 2 of the eruption. The red line is the cumulative V_G for the analysis period (Phases 1 and 2), taken from Fig. 7a, and the gray area corresponds to the cumulative 95% confidence level taken from Fig. 7a. The blue circles are the SAR-estimated V_D time series (modified from NIED (2018))

where $\boldsymbol{H_{dep}}$ and $\boldsymbol{H_{cap}}$ represent the smoothing matrices that provide the temporal parameter gradients for the depth and pressure change, respectively. We calculated the maximum likelihood based on Segall and Matthews (1997) and obtained the optimal hyperparameter values when the maximum likelihood was minimized:

$$(\textit{Maximum likelihood}) = \sum_{k=1}^{S} log|\boldsymbol{V}_k| + Slog\left[\sum_{k=1}^{S} \boldsymbol{v}_k^T \boldsymbol{V}_k^{-1} \boldsymbol{v}_k\right] \tag{11}$$

where S is the total number of epochs, $\boldsymbol{V}_k$ is the covariance matrix, and $\boldsymbol{v}_k$ is prediction residual, which is the difference between the observed data at time t_k and that predicted by the state-space vector conditioned using data up to time t_{k-1}. However, because the different parameter values in this study did not change the maximum likelihood much, we also determined the optimal

hyperparameter values by checking the calculated time series in Eq. (8) to verify the results of Eq. (11).

Deformation source time series

The results of the time-dependent inversion analysis for the Phase 1–Phase 2 period are shown in Fig. 7, and the time series of the observed and calculated values for each station are provided in Additional file 1: Fig. S3. The depth time series of the deflation source indicates that the source ascended from 11 to 7 km bsl during Phase 1, although the error is large at the beginning of the analysis period, and then gradually descended to around 8 km bsl during Phase 2 (Fig. 7a). The volume change decreased at almost the same rate (− 50,000 to − 80,000 m^3/h) during Phase 1, followed by a sudden increase in the rate of deflation at around 06:00 on 6 March (boundary between Phase 1 and Phase 2) that reached a stable peak from the afternoon of 6 March to the morning of 7 March, and then decreased to the initial rate of deflation by the morning of 8 March. The optimal values of the hyperparameters are found to be $\alpha_{dep} = \alpha_{cap} = 0.001$ (Additional file 1: Fig. S4). Although the number of strain data is low compared with that of the tilt data, the results of this inversion analysis reproduce the decrease in the |E2/E1| ratio during Phase 1 at ISA (Fig. 7b), which indicates that the calculation was able to account for the strain change. We consider these results reliable because the depth and volume changes exhibit the same trends for various initial values and hyperparameters in the inversion.

Discussion

Comparison of the geodetic volume change and extruded lava volume

We compare our estimated geodetic volume change during Phases 1 and 2 with the SAR-derived volume change of the lava dome (NIED 2018) during the same time period. The lava dome DRE volume time series (V_D) is larger than the estimated geodetic volume change results (V_G) at all three times when the SAR-derived volume changes were calculated during Phases 1 and 2 (Fig. 8). This variation between the deeper geodetic volume changes and surface-based lava dome volume changes is consistent with the fact that the magma in the magma reservoir is compressible (e.g., Segall 2010).

Kirishima magma plumbing system and ascending deflation source model

Here we incorporate seismic constraints on the Kirishima magma plumbing system to further refine the proposed magma plumbing system during the 2018 Shinmoe-dake eruption. Various seismic studies have imaged compressional-wave low-velocity regions (Yamamoto and Ida 1994), shear-wave low-velocity regions (Nagaoka et al. 2019), and seismic reflection surfaces (Mikada 1996) at 10–15 km bsl. We therefore assume that another magma reservoir exists below source A at 10–15 km bsl, which we define as reservoir B. Note that we use the term "reservoir" for B instead of "source" because its shape is not clearly defined. Reservoir B coincides with the depth at which the deflation source begins to ascend during Phase

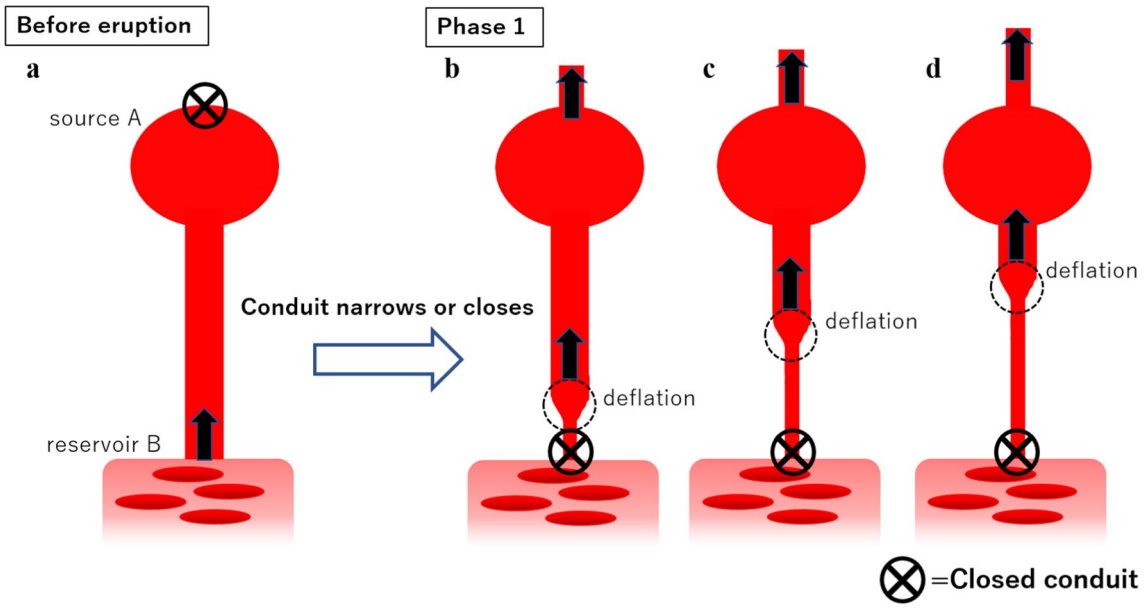

Fig. 9 Model of the ascending deflation source mechanism. **a** Before the eruption. **b**, **c**, and **d** During Phase 1 (14:00 on 5 March to 06:00 on 6 March)

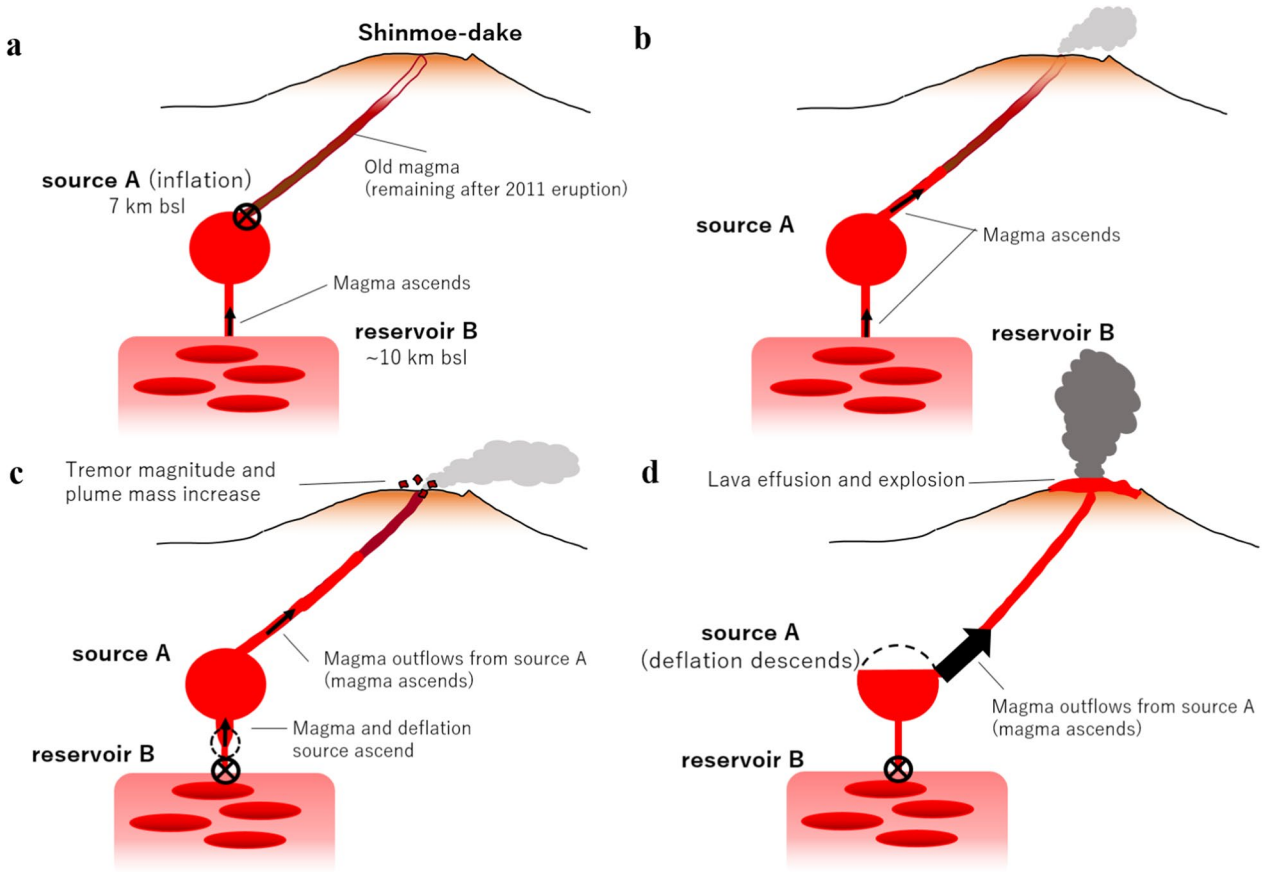

Fig. 10 Model of the magma ascent mechanism. **a** Before the 2018 Shinmoe-dake eruption. **b** 1 March (start of eruption) to 5 March (before Phase 1). **c** During Phase 1 (14:00 on 5 March to 06:00 on 6 March). **d** During Phase 2 (06:00 on 6 March to 12:00 on 8 March)

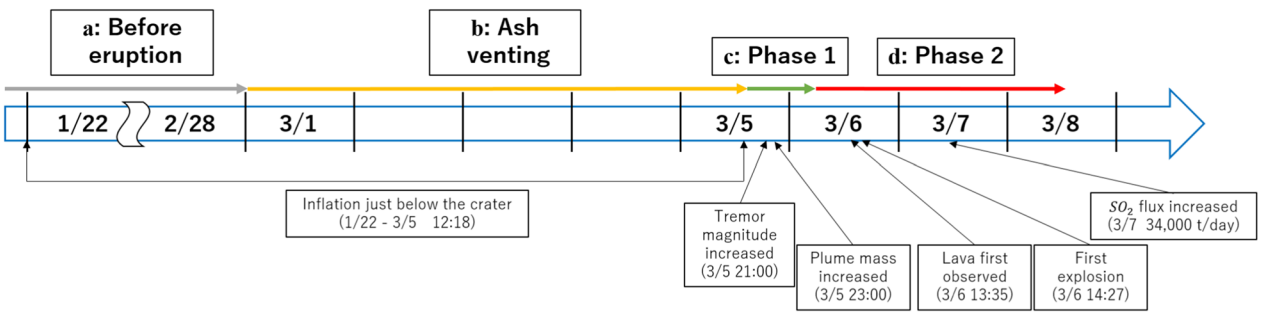

Fig. 11 Timeline of volcanic activity during the early stages of the 2018 Shinmoe-dake eruption. **a** to **d** refer to the presented magma ascent mechanisms in Fig. 10

1 of the time-dependent inversion analysis. Therefore, we estimate that the deflation source ascended from reservoir B to source A during Phase 1.

We propose the following model for the ascending deflation source during Phase 1. Magma is supplied from reservoir B to source A before the deflation source begins to ascend (Fig. 9a). The conduit above reservoir B then narrows during Phase 1, resulting in a reduced magma supply from reservoir B to source A (Fig. 9b). The magma in the conduit continues to ascend toward source A because of its steady buoyancy, but the supply flux from reservoir B is greatly reduced due to the narrowing conduit, resulting in the onset of decompression from depth. Magma continues to ascend, causing the deflation source

to ascend toward source A (Fig. 9c and d). Although it is possible that the conduit in the upper part of reservoir B becomes completely closed during this process, it is difficult to estimate whether the magma supply completely ceases during the 2018 eruption using the limited observations in this study.

Mechanism of pressure source movement

Before an eruption

We first describe the magma plumbing system of the Kirishima volcanic group. Two magma reservoirs, source A and reservoir B, exist at around 7 and 11 km bsl, respectively, beneath the Kirishima volcanic group (Fig. 10a). The conduit between source A and Shinmoedake crater is closed before a given eruption, whereas source A continues to receive magma from reservoir B. In fact, GNSS observations indicated inflation at around 7 km bsl from about July 2017 until just before the 2018 eruption (JMA 2018; GSI 2018). The inflation and deflation of source A during periods of volcanic quiescence are controlled by the magma supply from reservoir B.

Start of the 2018 eruption, prior to Phase 1

The start of the 2018 eruption was coincident with the opening of the dike (conduit) from source A to Shinmoedake crater, thereby allowing the ascent of magma toward the surface. This led to the ejection of the remnants of the 2011 eruption that had remained in the crater, resulting in continuous ash venting from 1 to 5 March (Fig. 10b). This is based on the assertion by Matsumoto and Geshi (2021) that the 1–5 March activity was emitting magma that was emplaced during the 2011 eruption. Furthermore, there were interferometric synthetic aperture radar (InSAR) observations of inflatable crustal deformation just below the crater during the 22 January–5 March 2018 period (Fujiwara et al. 2018). This crustal deformation can be explained by the opening of a dike, with an estimated volume change of 4.8×10^4 $m^3\sim700$ m below the crater (Additional file 1: Fig. S5). The ascent of this residual material (volcanic fluid), which was mainly from the 2011 eruption, is considered to be captured by the InSAR observations as crustal deformation. It is important to note that the observed deformation in the InSAR image (until 12:18 on 5 March) occurred up to just before Phase 1, which indicates that the dike opened as the precursor of a clear eruptive process (Fig. 11).

Phase 1

The magma supply from reservoir B to source A, which had persisted since before the eruption, began to decrease as the conduit above reservoir B began to narrow. Magma continued to ascend in the conduit owing to buoyancy, which is observed in the crustal deformation as the ascent of a deflation source (Fig. 10c); this is the Phase 1 mechanism that is described in the "Kirishima magma plumbing system and ascending deflation source model" subsection. Although magma is injected into the base of source A, the crustal movement can be explained by the movement of a single deflation source when approximately the same amount of magma outflow from source A is considered.

Phase 2. The ascending deflation source then reaches source A. The magma supply from below source A is now negligible, such that the deflation of a single pressure source (source A) can be considered (Fig. 10d). The rate and amount of deflation are both about one order of magnitude greater than those during Phase 1, with the magma ascent to the surface causing the lava effusion and explosive eruptions in the crater (Fig. 11). This magma outflows from source A, causing the center of the deflation source to descend to around 8 km bsl.

We then focus on the properties of the conduit that connects source A to the crater. Source A is located at 7 km bsl, such that the magma must ascend through a long conduit to the surface; however, we have not found any observations of either crustal deformation or tremors occurring along this conduit before and/or during the eruption. The lack of observations does not mean that there was no deformation within the conduit; however, any deformation must have been extremely small. Furthermore, the short lag time between the deflation of source A and the eruption suggests that the magma was able to quickly ascend through the conduit relatively unimpeded, with lava effusion and explosive activity only occurring after the magma ascended from source A. A slight deflation of source A during the preliminary stage of the eruption likely propagated directly through the conduit and caused the dike intrusion just beneath the crater, as indicated in the InSAR observations. Therefore, these observations suggest that the conduit had been filled with fluid magma since the 2011 eruption, such that the magma ascended smoothly through the conduit without any deformation.

The results of the geodetic analysis in this study suggest that the magma ascent and deflation began at depth prior to the visual observations of lava effusion. Although this time scale was short, being within one day of the visual observations, the highly accurate continuous strain and tilt observations around Shinmoe-dake made it possible to estimate detailed temporal changes in the pressure source.

Differences between the 2011 and 2018 eruptions

Here, we focused our analysis on the strain changes at ISA during the 2018 eruption; however, we did not

observe strain changes preceding either the sub-Plinian eruptions or lava effusion during the 2011 eruption (see Yamazaki et al. (2013) for the details of the 2011 eruption). This suggests that the 2011 and 2018 eruptions were caused by different magma ascent mechanisms.

Petrological studies have suggested that the 2011 eruption was caused by the mixing of mafic magma ascending from a magma reservoir around 8 km bsl (source A in this study) and silicic magma around 5 km bsl (Suzuki et al. 2013; Saito et al. 2023). The mixed magma that did not erupt in 2011 remained in the subsurface, and the magma that reached chemical equilibrium erupted during the 2018 eruption; Saito et al. (2023) attributed this eruption of 2011 materials to the injection of magma into the 8 km bsl magma reservoir. Therefore, the results of the present study provide geodetic support for the petrological inferences of different magmatic ascent processes during the 2011 and 2018 eruptions.

Conclusions

We analyzed the strain and tilt time series that were recorded during the 2018 Shinmoe-dake eruption to elucidate the magma ascent mechanism. The intensity of the eruption peaked during the 6–8 March period, which was marked by lava dome formation in the crater and frequent explosive eruptions. Previous studies have shown a distinct change in the tiltmeter observations from around 09:00 on 6 March to 12:00 on 8 March, thereby suggesting that the lava effusion occurred as the pressure source deflated. However, the strain data analysis in this study indicated that the crustal deformation caused by the deflation of the pressure source began about 19 h earlier, at around 14:00 on 5 March, and continued until 12:00 on 8 March. We divided this period into Phases 1 and 2 based on the changes in the |E2/E1| strain ratio and performed a time-dependent inversion analysis of the pressure source throughout this period. The inversion results showed that the deflation source ascended from ~ 11 to 7 km bsl during Phase 1, and then gradually descended from 7 to 8 km bsl during Phase 2. This study provides the first evidence of an ascending deflation source during the early stage of the 2018 eruptions, with this deflation source initiating at a deeper location than the source that was estimated during lava effusion. We attribute the ascension of the deflation source during Phase 1 to the narrowing (and possible closure) of the conduit from reservoir B, whereas the slight deepening of the deflation source during Phase 2 is attributed to the increased magma outflow from source A to the crater. The results of this study suggest that magma can ascend from depth to the surface within a short time period, thereby providing new insights into potential eruption mechanisms.

Abbreviations

InSAR	Interferometric Synthetic Aperture Radar
EnKF	Ensemble Kalman Filter
GNSS	Global Navigation Satellite System
JMA	Japan Meteorological Agency
NIED	National Research Institute for Earth Science and Disaster Prevention
VDSVD	Volcanological Division, Seismological and Volcanological Department, Japan Meteorological Agency
ISA	Isa-Yoshimatsu observatory, operated by Kyoto University
KITK	Takachihokawara observatory, operated by Japan Meteorological Agency
KION	Oonamiikenansei observatory, operated by Japan Meteorological Agency
KRMV	Manzen observatory, operated by the National Research Institute for Earth Science and Disaster Prevention
KRHV	Hinamoridai observatory, operated by the National Research Institute for Earth Science and Disaster Prevention
EBN	Ebino meteorological observation site, operated by Japan Meteorological Agency
YSMT	Yoshimatsu meteorological observation site, operated by Kagoshima Prefecture
FDMO	Fukuoka District Meteorological Observatory of Japan Meteorological Agency
KLMO	Kagoshima Local Meteorological Observatory of Japan Meteorological Agency
DRE	Dense-rock-equivalent
MCMC	Markov Chain Monte Carlo
GSI	Geospatial Information Authority of Japan

Supplementary Information

The online version contains supplementary material available at https://doi.org/10.1186/s40623-023-01895-4.

Additional file 1: Fig. S1 Comparison of strain and tilt data before and after tidal, precipitation and instrument drift corrections. Gray lines are the original time series data. Colored lines are corrected data after removal of the tidal, precipitation and instrument drift components. Gray bars at the bottom of each panel represent the hourly precipitation measurements at Yoshimatsu (YSMT, Fig. 1; upper panel) and Ebino (EBN, Fig. 1; lower panels). Black dashed lines denote the start and end times of the defined crustal deformation in this study (14:00 on 5 March to 12:00 on 8 March). **Fig. S2** Estimated depth and volume change for a simulated source using EnKF. Red lines are calculated values, and blue lines are simulated values. Gray areas correspond to the 95% confidence level. **Fig. S3** Observed (black) and calculated (red) strain and tilt time series at all sites after the time-dependent inversion. The error bars at ISA and the tilt stations are 1×10^{-8} and 2×10^{-8}, respectively. The dashed line marks the boundary between Phases 1 and 2 of the eruption (06:00 on 6 March). **Fig. S4** Maximum likelihood of α_{dep} (upper) and α_{cap} (lower) for each tested hyperparameter value. The maximum likelihood was the smallest when $\alpha_{dep} = 0.1$ and $\alpha_{cap} = 0.001$. However, $\alpha_{dep} = \alpha_{cap} = 0.01$ were used as the optimal values in this study. **Fig. S5** Surface displacement maps from the InSAR analysis of the 22/01/2018 12:18–05/03/2018 12:18 ALOS-2 image pair. Hot areas indicate displacements toward the satellite, and cold areas indicate displacements away from the satellite. **a** Observed surface displacements. **b** Modeled surface displacements. **c** Residuals between the model and observations.

Acknowledgements

We used data from the Japan Meteorological Agency and the National Research Institute for Earth Science and Disaster Prevention for the tiltmeter data analysis (KITK, KRMV, and KRHV). The KION tiltmeter data and camera image data were provided by the Fukuoka District Meteorological Observatory (https://www.data.jma.go.jp/fukuoka/index.html). We used precipitation data from the Kagoshima Prefecture and Japan Meteorological Agency. We thank H. Munekane for providing the crustal deformation analysis software

(pydeform) and K. Aizawa for insightful comments that improved the quality of the paper. The figures were generated using the Generic Mapping Tools (GMT) software package (Wessel and Smith, 1991).

Author contributions
KY designed the research, performed the analyses, and wrote the article. TM and HS contributed to the interpretation of the results. KY and YY contributed to the interpretation of the results and data acquisition. SK contributed to the data acquisition and assisted in the inspection of the data. SF analyzed the InSAR data and provided the surface displacements. All of the authors read and approved the final manuscript.

Funding
This study was supported by Kyoto University and the Ministry of Education, Culture, Sports, Science and Technology (MEXT) of Japan, under its Earthquake and Volcano Hazards Observation and Research Program.

Availability of data and materials
The tilt data, with the exception of the KION data, are available from the Crustal Deformation Database (https://nipe.sci.hokudai.ac.jp/db/login.php, in Japanese). The EBN precipitation data are available from the JMA website (https://www.data.jma.go.jp/gmd/risk/obsdl/index.php, in Japanese). The BAYTAP-G tidal component program is available from the National Institute of Advanced Industrial Science and Technology website (https://gbank.gsj.jp/wellweb/GSJ/water/analysis/, in Japanese). The other datasets are not publicly available due to the prior use rights of the data acquirer, but they are available from the corresponding author on reasonable request.

Declarations

Ethics approval and consent to participate
Not applicable.

Consent for publication
Not applicable.

Competing interests
The authors declare that they have no competing interests.

Author details
[1]Department of Earth and Planetary Sciences, Graduate School of Science, Kyushu University, Motooka 744, Nishi-Ku, Fukuoka 819-0395, Japan. [2]Institute of Seismology and Volcanology, Faculty of Science, Kyushu University, Fukuoka 819-0395, Japan. [3]Disaster Prevention Research Institute, Miyazaki Observatory, Kyoto University, Miyazaki 889-2161, Japan. [4]Geospatial Information Authority of Japan, Ibaraki 305-0811, Japan.

Received: 14 February 2023 Accepted: 4 September 2023
Published online: 20 September 2023

References

Asia Air Survey Co. Ltd, National Institute of Advanced Industrial Science and Technology, the Earthquake Research Institute, the Kumamoto university (2018) Volumetric changes in lava associated with the 2018 eruption of Mt. Kirishima (Shinmoe-dake). Paper presented at a meeting of Coordinating Committee for Prediction of Volcanic Eruption, 20 Jun 2018. (in Japanese) https://www.data.jma.go.jp/svd/vois/data/tokyo/STOCK/kaisetsu/CCPVE/shiryo/141/141_01-2.pdf

Bonforte A, Bonaccorso A, Guglielmino F, Palano M, Puglisi G (2008) Feeding system and magma storage beneath Mt. Etna as revealed by recent inflation/deflation cycles. J Geophys Res 113:B05406. https://doi.org/10.1029/2007JB005334

Fukuoka District Meteorological Observatory and the Kagoshima Local Meteorological Observatory of Japan Meteorological Agency (2018). Explanatory material on volcanic activity of Mt. Kirishima (Shinmoe-dake). Available via DIALOG. https://www.data.jma.go.jp/svd/vois/data/tokyo/STOCK/monthly_v-act_doc/monthly_vact.php Accessed 5 Jan 2023

Fukuoka District Meteorological Observatory and the Kagoshima Local Meteorological Observatory of Japan Meteorological Agency (2023) Explanatory material on volcanic activity of Mt. Kirishima. Available via DIALOG. https://www.data.jma.go.jp/vois/data/tokyo/STOCK/activity_info/505.html Accessed 10 February 2023. (in Japanese)

Fujiwara S, Yarai H, Kobayashi T, Morishita Y, Ozawa S (2018) Crustal deformation around Kirishima mountains associated with 2017–2018 eruptions. Paper presented at the volcanological society of Japan 2018 fall meeting, Akita University, Akita, 26–30 September 2018. (in Japanese) https://doi.org/10.18940/vsj.2018.0_180

Genco R, Ripepe M (2010) Inflation-deflation cycles revealed by tilt and seismic records at Stromboli volcano. Geophys Res Lett 37:L12302. https://doi.org/10.1029/2010GL042925

Geospatial Information Authority of Japan (2018) Crustal Deformations around Kirishima Volcano. Rep Coordinating Comm Prediction Volcan Eruption 130:324–347. (in Japanese) https://www.data.jma.go.jp/svd/vois/data/tokyo/STOCK/kaisetsu/CCPVE/Report/130/kaiho_130_44.pdf

Ishiguro M, Sato T, Tamura Y, Ooe M (1984) Tidal data analysis—an introduction to BAYTAP -. Proc Inst Stat Math 32:71–85

Japan Meteorological Agency (2018) Volcanic activity of Kirishima volcano -February 1, 2018—May 31, 2018-. Rep Coordin Comm Prediction Volcan Eruption 130:213–284

Kato K, Yamasato H (2013) The 2011 eruptive activity of Shinmoedake volcano, Kirishimayama, Kyushu, Japan—overview of activity and volcanic alert level of the japan meteorological agency -. Earth Planets Space 65:489–504. https://doi.org/10.5047/eps.2013.05.009

Kimura K, Tsuyuki T, Suganuma I, Hasegawa H, Misu H, Fujita K (2015) Rainfall Correction of Volumetric Strainmeter Data by Tank Models. Q J Seismol 78:93–158. (in Japanese with English abstract) https://www.jma.go.jp/jma//kishou/books/kenshin/vol78p093.pdf

Matsumoto K, Geshi N (2021) Shallow crystallization of eruptive magma inferred from volcanic ash microtextures: a case study of the 2018 eruption of Shinmoedake volcano. Japan Bull Volcanol 83:31. https://doi.org/10.1007/s00445-021-01451-6

McTigue DF (1987) Elastic Stress and Deformation Near a Finite Spherical Magma Body: Resolution of the Point Source Paradox. J Geophys Res 92:12931–12940. https://doi.org/10.1029/JB092iB12p12931

Mikada H (1996) A Seismic Reflection Analysis on Refraction Data from the 1994 Kirishima Explosion Experiment, Bull Volcanol Soc Jpn, 41:159–170. (in Japanese with English abstract) https://doi.org/10.18940/kazan.41.4_159

Mogi K (1958) Relations between the Eruptions of Various Volcanoes and the Deformations of the Ground Surfaces around them. Bull Earthq Res Inst Univ Tokyo 36:99–134

Munekane H, Oikawa J, Kobayashi T (2016) Mechanisms of step-like tilt changes and very long period seismic signals during the 2000 Miyakejima eruption: Insights from kinematic GPS. J Geophys Res 121:2932–2946. https://doi.org/10.1002/2016JB012795

Munekane H, Oikawa J (2017) Estimation of volcano deformation source parameters by the time-dependent inversion. Paper presented at the volcanological society of Japan 2017 fall meeting, Kumamoto University, Kumamoto, 21–24 September 2017. (in Japanese) https://doi.org/10.18940/vsj.2021.0_7

Nagaoka Y, Nishida K, Aoki Y, Takeo M, Ohkura T, Yoshikawa S (2019) Imaging of the magma pathway beneath Kirishima volcanoes by seismic interferometry. Paper presented at the Japan Geoscience Union Meeting 2019, Makuhari Messe, Chiba, 26–30 May 2019. (in Japanese) https://confit.atlas.jp/guide/event-img/jpgu2019/SSS17-P02/public/pdf?lang=ja

Nakada S, Nagai M, Kaneko T, Suzuki Y, Maeno F (2013) The outline of the 2011 eruption at Shinmoe-dake (Kirishima), Japan. Earth Planets Space 65:475–488. https://doi.org/10.5047/eps.2013.03.016

Nakamichi H, Aoyama H (2016) Eruption Process Inferred from Multi-parameter Geophysical Observations, Bull Volcanol Soc Jpn 61:119–154. (in Japanese with English abstract) https://doi.org/10.18940/kazan.61.1_119

Nakao S, Morita Y, Yakiwara H, Oikawa J, Ueda H, Takahashi H, Ohta Y, Matsushima T, Iguchi M (2013) Volume change of the magma reservoir relating to the 2011 Kirishima Shinmoe-dake eruption—charging, discharging and recharging process inferred from GPS measurements. Earth Planets Space 65:505–515. https://doi.org/10.5047/eps.2013.05.017

National Research Institute for Earth Science and Disaster Prevention (2018) Lava changes in Shinmoe-dake crater by SAR. Paper presented at a

meeting of Coordinating Committee for Prediction of Volcanic Eruption, 20 Jun 2018. (in Japanese) https://www.data.jma.go.jp/svd/vois/data/tokyo/STOCK/kaisetsu/CCPVE/shiryo/141/141_01-2.pdf
Saito G, Oikawa T, Ishizuka O (2023) Magma ascent and degassing processes of the 2011 and 2017–18 eruptions of Shinmoedake in Kirishima volcano group, Japan, based on petrological characteristics and volatile content of magmas. Earth Planets Space 2023:75–89. https://doi.org/10.1186/s40623-023-01836-1
Segall P (2010) Earthquake and volcanic deformation. Princeton Univ, Princeton
Segall P, Matthews M (1997) Time dependent inversion of geodetic data. J Geophys Res 102:22391–22409. https://doi.org/10.1029/97JB01795
Suzuki Y, Yasuda A, Hokanishi N, Kaneko T, Nakada S, Fujii T (2013) Syneruptive deep magma transfer and shallow magma remobilization during the 2011 eruption of Shinmoe-dake, Japan—constraints from melt inclusions and phase equilibria experiments. J Volcanol Geotherm Res 257:184–204. https://doi.org/10.1016/j.jvolgeores.2013.03.017
Tajima Y, Oikawa J, Kobayashi T, Yasuda A (2022) Middle to long-term magma producing activities and the plumbing system of Shinmoedake Kirishima Volcano: toward a unified understanding based on volcanic products analyses and geophysical observations. Bull Volcanol Soc Jpn 67:45–68. https://doi.org/10.18940/kazan.67.1_45
Tanner L, Calvari S (2012) Volcanoes: Windows on the Earth. The New Mexico Museum of Natural History and Science, Albuquerque.
Ueda H, Fujita E, Ukawa M, Yamamoto E (2010) Automated technique for anomalous volcanic crustal deformation detection and source estimation by using real time tiltmeter data. Rep Nat Res Inst for Earth Sci Disast Prev 76:21–32
Ueda H, Kozono T, Fujita E, Kohno Y, Nagai M, Miyagi Y, Tanada T (2013) Crustal deformation associated with the 2011 Shinmoe-dake eruption as observed by tiltmeters and GPS. Earth Planets Space 65:517–525. https://doi.org/10.5047/eps.2013.03.001
Volcanological Division, Seismological and Volcanological Department, Japan Meteorological Agency (2014) Installation of New Volcano Monitoring Systems for 47 Volcanoes in Japan. Q J Seismol 77:241–310
Wessel P, Smith WHF (1991) Free software helps map and display data. EOS Trans AGU 72:441–446. https://doi.org/10.1029/90EO00319
Williams CA, Wadge G (1998) The effects of topography on magma chamber deformation models: Application to Mt. Etna and radar interferometry. Geophys Res Lett 25:1549–1552. https://doi.org/10.1029/98GL0113
Williams CA, Wadge G (2000) An accurate and efficient method for including the effects of topography in three-dimensional elastic models of ground deformation with applications to radar interferometry. J Geophys Res 105:8103–8120. https://doi.org/10.1029/1999JB900307
Yamamoto K, Ida Y (1994) Three-dimensional p-wave velocity structure of Kirishima volcanoes using regional seismic events. Bull Earthq Res Inst Univ Tokyo 69:267–289
Yamazaki K, Teraishi M, Ishihara K, Komatsu S, Kato K (2013) Subtle changes in strain prior to sub-Plinian eruptions recorded by vault-housed extensometers during the 2011 activity at Shinmoe-dake, Kirihima volcano, Japan. Earth Planets Space 65:1491–1499. https://doi.org/10.5047/eps.2013.09.005
Yamazaki K, Yamashita Y, Komatsu S (2020) Vault-housed extensometers recorded a rapid initial pulse before precursory magma reservoir inflation related to the 2011 eruption of Shinmoe-dake. Japan Earth Planets Space 83:72. https://doi.org/10.1186/s40623-020-01211-4

Publisher's Note